
Towards Realistic Data Generation for Real-World Super-Resolution

Long Peng^{1,2*} Wenbo Li^{2†} Renjing Pei² Jingjing Ren³ Yang Wang^{1†}
Yang Cao¹ Zheng-Jun Zha¹

¹ University of Science and Technology of China

² Huawei Noah's Ark Lab

³ The Hong Kong University of Science and Technology (Guangzhou)

Abstract

Existing image super-resolution (SR) techniques often fail to generalize effectively in complex real-world settings due to the significant divergence between training data and practical scenarios. To address this challenge, previous efforts have either manually simulated intricate physical-based degradations or utilized learning-based techniques, yet these approaches remain inadequate for producing large-scale, realistic, and diverse data simultaneously. In this paper, we introduce a novel Realistic Decoupled Data Generator (RealDGen), an unsupervised learning data generation framework designed for real-world super-resolution. We meticulously develop content and degradation extraction strategies, which are integrated into a novel content-degradation decoupled diffusion model to create realistic low-resolution images from unpaired real LR and HR images. Extensive experiments demonstrate that RealDGen excels in generating large-scale, high-quality paired data that mirrors real-world degradations, significantly advancing the performance of popular SR models on various real-world benchmarks.

1 Introduction

Real-world image Super-Resolution (Real SR) is a fundamental problem in image processing, aiming to enhance the resolution and quality of images in real-world scenarios [1, 2, 3, 4, 5, 6, 7, 8, 9, 10, 11, 12, 13, 14, 15, 16, 17, 18, 19, 20, 21, 22]. It has a wide range of applications across various fields, including photography [18] and medical imaging [23], which enhance human visual perception and the robustness of vision systems [24, 25, 26, 27]. However, traditional bicubic-interpolation-based Real SR methods have proven less effective in complex real-world scenarios due to the significant discrepancy between the bicubic pattern and real degradation [1, 3, 28, 29, 30]. Consequently, substantial efforts have been directed towards developing methods for generating more realistic data to improve the generalization ability of Real SR models [28, 31, 32, 33, 34, 35, 36, 37, 38].

To explore what kind of data contributes most to the SR model's capability, we synthesize different sets of training data using [39] and evaluate the performance of FSRCNN [40]. As shown in the top left of Figure 1, the red triangles represent test samples of the target domain, while rectangular boxes indicate training sets with different blur kernels and noise levels. The results clearly demonstrate that the closer the training data distribution is to the test data, the better the model's performance. This underscores the importance of designing a method that can adaptively generate accurate data for different target domains. Therefore, an ideal data generation system for Real SR should meet the

*Work done when the first author interned at Huawei Noah's Ark Lab.

†Wenbo Li and Yang Wang are the corresponding authors.

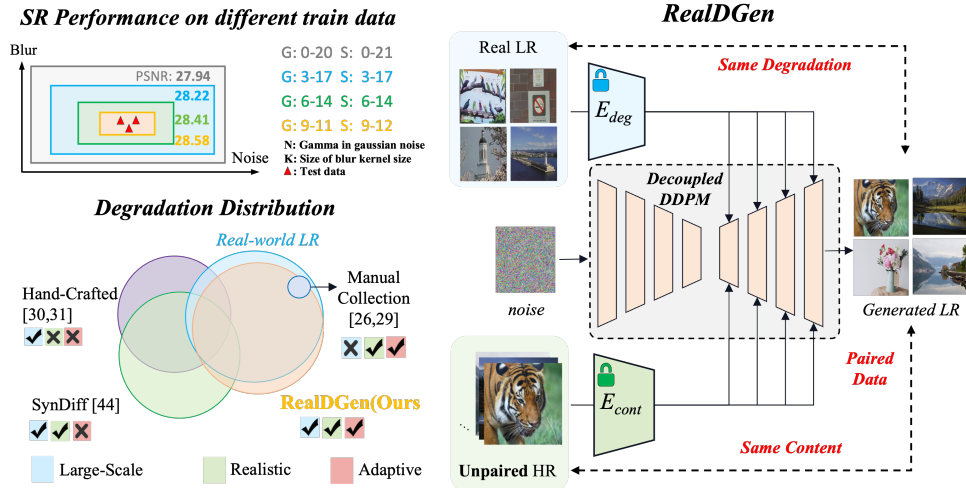


Figure 1: The top left and bottom left are SR performance on different train data and degradation distribution of different methods. The right is our unsupervised data generation framework RealDGen.

following criteria: **I) Large-scale**, to satisfy the extensive data requirements for training deep learning models [41, 42, 43, 44]; **II) Realistic**, to enable Real SR models to accurately learn the characteristics of real-world degradation [28, 31, 32]; and **III) Adaptive**, to flexibly generate data with arbitrary given degradation patterns, improving generalization in target domains [3, 34].

Existing data generation methods for Real SR [28, 31, 32, 33, 42, 45, 46, 47, 48, 49], as shown in the bottom left of Figure 1, can be broadly categorized into the following: **a) Manual Collection via Focal Length Adjustment**: This approach involves using digital single-lens reflex cameras (DSLRs) with varying focal lengths to capture images, followed by alignment [28, 31]. While it can produce realistic paired data, it is labor-intensive and often results in scene monotony and image misalignment, failing to meet the large-scale data requirement. **b) Hand-Crafted Physical-Based Degradation Modeling**: This method employs various degradation models (e.g., noise, blur, bicubic, JPEG) applied in single-order or higher-order combinations [32, 33]. Although efficient in generating large data quantities, the synthetic data often fails to accurately reflect the complex degradation patterns of real-world images, and its lack of adaptability to specific domains limits effectiveness. **c) Learning-Based Methods**: Techniques involving Generative Adversarial Networks (GANs) [35, 45] and diffusion models [46] are proposed to simulate realistic real-world degradation for low-resolution (LR) images. While these methods produce more realistic data compared to hand-crafted approaches, they often struggle to generalize to new and diverse domains, limiting their applicability in real-world scenarios. In summary, existing data generation methods face challenges in achieving both realism and adaptability: tailoring models to specific target domains may hinder their adaptability to new domains, and vice versa. Overcoming these challenges is crucial for advancing the field of Real SR.

In this paper, we introduce the unsupervised learning framework Realistic Decoupled Data Generator (RealDGen) to meet the large-scale, realistic, and adaptive data generation criteria. RealDGen enhances degradation realism and content fidelity by separately modeling content and degradation through unsupervised learning and integrating them into a diffusion model to generate paired data. The training involves two steps: first, pre-training degradation and content extractors using contrastive and reconstruction learning strategies to improve representation robustness; second, using these pre-trained extractors to condition the diffusion model with real LR degradation and content representations. To improve generalization to unknown LR distributions, the partial parameters of the extractors are fine-tuned. During data generation, unpaired HR and real LR images are used to extract content and degradation representations, which are then combined in the diffusion model. This process produces data that marries HR content with arbitrary LR degradation, improving adaptability to new domains. Extensive experiments show that RealDGen outperforms previous methods in generating realistic paired data and enhancing the performance of SR models in real-world scenarios.

The contributions of this paper can be summarized as follows:

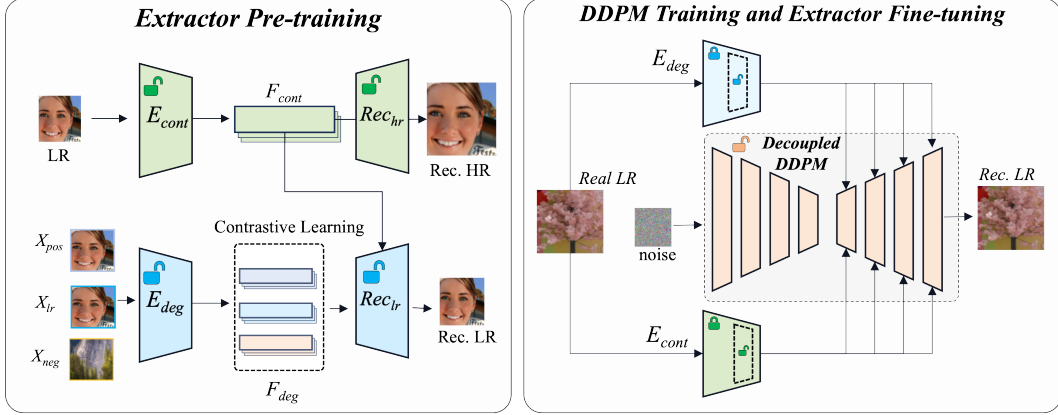


Figure 2: An overview of our unsupervised training pipeline. We first train on the content and degradation extractors, then train Decoupled DDPM while fine-tuning the partial parameters of the extractors. RealDGen adaptively generates realistic LR images with arbitrary given real LR and unpaired HR conditions.

- We propose a novel unsupervised Realistic Decoupled Data Generator (RealDGen) to adaptively generate large-scale, realistic, and diverse data for real-world super-resolution.
- We introduce well-designed content and degradation extraction strategies and a novel content-degradation decoupled diffusion model to generate realistic LR with arbitrary unpaired LR and HR conditions.
- Compared with previous methods, our method significantly advances the generalization ability of popular SR models, achieving the best performance on real-world benchmarks.

2 Method

In this paper, we introduce a novel Realistic Decoupled Data Generator (RealDGen) for real-world super-resolution to adaptively generate large-scale, realistic, and diverse real paired data. In particular, well-designed content and degradation extractor learning strategies are proposed to capture robust content and degradation representations in the real world. A novel content-degradation decoupled diffusion model is proposed to generate realistic LR with arbitrary unpaired LR and HR conditions. The training process is divided into two distinct phases: (a) Content and Degradation Extractor Pre-training and (b) Decoupled DDPM Training and Extractor Fine-tuning, as shown in Figure 2.

2.1 Content and Degradation Extractor Pre-training

To capture content and degradation representations, we propose dedicated degradation and content extractors, denoted as E_{deg} and E_{cont} , respectively. We employ reconstruction learning for training E_{cont} , as shown in Figure 2 (a). Specifically, for a given high-resolution (HR) image $\mathcal{X} \in \mathbb{R}^{C \times H \times W}$, we degrade it to a low-resolution (LR) counterpart $\mathcal{X}_{lr} \in \mathbb{R}^{C \times h \times w}$ by Real-RSRGAN [33] degradation model \mathcal{D} with diverse synthetic degradations. Subsequently, E_{cont} is engaged to extract the content representation F_{cont} from \mathcal{X}_{lr} . Thereafter, a HR reconstruction network Rec_{hr} is harnessed to reconstruct the HR image $\hat{\mathcal{X}} \in \mathbb{R}^{C \times H \times W}$ from F_{cont} , as follows:

$$F_{cont} = E_{cont}(\mathcal{X}_{lr}), \hat{\mathcal{X}} = Rec_{hr}(F_{cont}). \quad (1)$$

The objective is to minimize the reconstruction loss \mathcal{L}_{rh} between the reconstructed image $\hat{\mathcal{X}}$ and the original high-resolution image \mathcal{X} , as follows:

$$\mathcal{L}_{rh} = \frac{1}{N} \sum_{i=1}^N (\hat{\mathcal{X}}_i - \mathcal{X}_i)^2, \quad (2)$$

where N denotes the batch size, which we set to 64. After training, E_{cont} learns a robust content representation under diverse synthetic degradations.

Algorithm 1 Decoupled DDPM Training

```

1: repeat
2:  $\mathbf{x}_{lr} \sim q(\mathbf{x}_{lr})$ 
3:  $t \sim \text{Uniform}(\{1, \dots, T\})$ 
4:  $\epsilon \sim \mathcal{N}(\mathbf{0}, \mathbf{I})$ 
5:  $\mathbf{F}_{\text{cont}} = E_{\text{cont}}(\mathbf{x}_{lr})$ 
6:  $\mathbf{F}_{\text{deg}} = E_{\text{deg}}(\mathbf{x}_{lr})$ 
7:  $\mathbf{c} = \mathcal{M}(\mathbf{F}_{\text{cont}}, \mathbf{F}_{\text{deg}})$ 
8: Take gradient descent step on
    $\nabla_{\theta} \|\epsilon - \epsilon_{\theta}(\sqrt{\bar{\alpha}_t}\mathbf{x}_0 + \sqrt{1 - \bar{\alpha}_t}\epsilon, \mathbf{c}, t)\|^2$ 
9: until converged

```

Algorithm 2 Data Generation

```

1:  $\mathbf{x}_{lr} \sim q(\mathbf{x}_{lr}), \mathbf{x}_{hr} \sim p(\mathbf{x}_{hr})$ 
2:  $\mathbf{c} = \mathcal{M}(E_{\text{deg}}(\mathbf{x}_{lr}), E_{\text{cont}}(\mathbf{x}_{hr}))$ 
3:  $\tau \sim \text{Uniform}(\{1, \dots, T\})$ 
4:  $\mathbf{x}_t = (\sqrt{\bar{\alpha}_t}\mathcal{D}(\mathbf{x}_{lr}) + \sqrt{1 - \bar{\alpha}_t}\epsilon), \epsilon \sim \mathcal{N}(\mathbf{0}, \mathbf{I})$ 
5: for  $t = \tau, \dots, 1$  do
6:  $\mathbf{z} \sim \mathcal{N}(\mathbf{0}, \mathbf{I})$  if  $t > 1$ , else  $\mathbf{z} = \mathbf{0}$ 
7:  $\mathbf{x}_{t-1} = \frac{1}{\sqrt{\bar{\alpha}_t}} \left( \mathbf{x}_t - \frac{1 - \bar{\alpha}_t}{\sqrt{1 - \bar{\alpha}_t}} \epsilon_{\theta}(\mathbf{x}_t, \mathbf{c}, t) \right) + \sigma_t \mathbf{z}$ 
8: end for
9: return  $\mathbf{x}_0$ 

```

Considering the variability of degradation in diverse scenarios and imaging devices in the real world, we advocate for contrastive learning to curate positive and negative samples for training E_{deg} , which guarantees the uniqueness of the degradation representations. Specifically, for a HR image $\mathcal{X} \in \mathbb{R}^{C \times H \times W}$, we generate an LR image $\mathcal{X}_{lr} \in \mathbb{R}^{C \times h \times w}$ by \mathcal{D} with parameter θ as the anchor \mathcal{X}_{anc} . We further obtain a set of negative samples $\mathcal{X}_{neg_i} \in \mathbb{R}^{C \times h \times w}$ by applying \mathcal{D} with different parameters θ_i to \mathcal{X} , and a set of positive samples $\mathcal{X}_{pos_i} \in \mathbb{R}^{C \times h \times w}$ by applying the degradation \mathcal{D} with same parameter θ to different HR images $\mathcal{X}'_i \in \mathbb{R}^{C \times H \times W}$, as follows:

$$\begin{aligned} \mathcal{X}_{neg} &= \{\mathcal{D}(\mathcal{X}, \theta_1), \mathcal{D}(\mathcal{X}, \theta_2), \dots, \mathcal{D}(\mathcal{X}, \theta_n)\} \\ \mathcal{X}_{pos} &= \{\mathcal{D}(\mathcal{X}'_1, \theta), \mathcal{D}(\mathcal{X}'_2, \theta), \dots, \mathcal{D}(\mathcal{X}'_n, \theta)\}. \end{aligned} \quad (3)$$

The objective is to minimize the contrastive loss \mathcal{L}_{cl} to drive E_{deg} learn the uniqueness of the degradation representations in LR images, suppressing the interruption of content, as follows:

$$\mathcal{L}_{cl} = \sum_{i=1}^n \max(0, d(E_{deg}(\mathcal{X}_{anc}), E_{deg}(\mathcal{X}_{pos_i})) - d(E_{deg}(\mathcal{X}_{anc}), E_{deg}(\mathcal{X}_{neg_i})) + margin), \quad (4)$$

where d symbolizes the L2 distance, n is the number of samples, and we empirically set n and $margin$ to 3 and 0.01, respectively. Furthermore, to drive E_{deg} to learn the complete degradation representations, we utilize the reconstruction learning strategy as aforementioned for supervising E_{deg} . Specifically, we utilize the pre-trained E_{cont} to learn the content representation of \mathcal{X}_{hr} and E_{deg} to learn the degradation representations of \mathcal{X}_{lr} . We then employ a low-resolution reconstruction network, Rec_{lr} , to combine these representations and reconstruct the LR image, $\hat{\mathcal{X}}_{lr}$, as follows:

$$\hat{\mathcal{X}}_{lr} = Rec_{lr}(E_{deg}(\mathcal{X}_{lr}), E_{cont}(\mathcal{X}_{hr})). \quad (5)$$

The objective is to minimize the reconstruction loss \mathcal{L}_{rl} to drive E_{deg} learn the completeness of the degradation representations as follows:

$$\mathcal{L}_{rl} = \frac{1}{N} \sum_{i=1}^N (\hat{\mathcal{X}}_{lr_i} - \mathcal{X}_{lr_i})^2. \quad (6)$$

After training with well-designed learning strategies, the proposed encoders effectively capture robust content and degradation representations. More details are provided in Section A.1 and Section A.2 of the appendix.

2.2 Decoupled DDPM Training and Extractor Fine-tuning

We introduce a content-degradation Decoupled Diffusion Probabilistic Model (Decoupled DDPM) to generate real LR images. In detail, given real LR images \mathcal{X}_{lr} from real-world q , we extract their content representation F_{cont} and degradation representation F_{deg} by pre-trained E_{cont} and E_{deg} , respectively. To enhance the generalization of E_{deg} and E_{cont} on unseen real distributions, partial parameters are fine-tuned, as shown in Figure 2. A modulation block \mathcal{M} is introduced to adequately incorporate degradation representation into the content, formulated as:

$$\mathbf{c} = \mathcal{M}(E_{deg}(\mathbf{x}_{lr}), E_{cont}(\mathbf{x}_{hr})). \quad (7)$$

Then, this fused image representation is utilized as a condition \mathbf{c} for training our Decouple DDPM to generate LR images. To make it clear, we illustrate the detailed training procedure of the Decouple DDPM, as shown in Algorithm 1. A detailed presentation of \mathcal{M} and fine-tuning is provided in Sections A.3, A.4 and A.5 of the appendix.

2.3 Data Generation

We propose a novel strategy to generate realistic LR images using unpaired LR and HR images by decoupling content and degradation. First, we extract the degradation representation from a real-world LR image and the content representation from an HR image. These representations are combined in the modulation module \mathcal{M} to serve as the condition \mathbf{c} for the diffusion model to generate LR images. The generated LR images retain the content of the HR image and the degradation of the real LR image, as shown on the right of Figure 1. To enhance fidelity, following [50], we denoise from an initial LR image \mathbf{x}_t with t steps of noise rather than from pure Gaussian noise. This initial LR image is degraded by \mathcal{D} . In Sec.3.4, we analyze the step number T . Details of our data generation pipeline are in Algorithm 2.

Although using content and degradation conditions improves the controllability and fidelity of Decoupled DDPM, the inherent stochasticity of the diffusion model [51, 52] can still introduce tiny artifacts and content distortion. To mitigate this, we propose a filtering mechanism. For each generated LR image, we re-extract content and degradation representations, then calculate the degradation error with the real LR image and the content error with the HR image. By selecting samples with the smallest errors, we reduce diffusion stochasticity and produce higher-fidelity LR images. More details will be presented in Section A.6 of the appendix.

3 Experiments and Analysis

3.1 Experiments Settings

Training Details. We have collected about 152,000 real low-resolution images from both public datasets [31, 28, 49] and those captured using smartphones. We train our extractors and Decouple DDPM on 16 NVIDIA V100 GPUs and set the learning rate and batch size to 1×10^{-4} and 16, respectively. More details of the training setting are presented in Section A.1 and A.3 of the appendix.

To ensure a fair comparison, we compare our approach with existing methods by using the widely-used DIV2K dataset [53] as content reference and real LR images as degradation reference to create the paired training data for training various popular SR models. To maintain a rigorous and fair comparison, we have maintained consistency in all experimental settings and environments, with the exception of data generation. We utilize the public BasicSR³ for training Real-SR methods with 16 NVIDIA V100 GPUs.

Compared Data Generation Methods. We compare our methods with some state-of-the-art real-world data generation methods, including Hand-Crafted Physical-Based Degradation Models (BSRGAN [32] and Real-ESRGAN [33]) and learning-based degradation diffusion models proposed by [46], denoted as SynDiff for convenience.

Real-SR Models. To comprehensively validate the effectiveness of the generated data, we carefully select four classic and representative backbone architectures for evaluation, including representative CNN-based model RRDB [54], representative transformer-based model SwinIR [55] and HAT [56], representative lightweight model SwinIR-L [55]. To be fair, we conduct comparative evaluations under consistent experimental conditions and settings. We utilize L1Loss [56, 55] and perception loss [33, 57, 54] for training PNSR-oriented and Perception-oriented real SR models, respectively.

Metrics. For the PNSR-oriented Real SR model, we adopt PSNR [58] and SSIM [59] to quantitatively evaluate the performance. For the perception-oriented Real-SR model, we adopt LPIPS [60] and FID [61] to quantitatively evaluate the performance. DISTS [62] and CLIP-Score [63] are further introduced to evaluate the accuracy of generated data. Note that the higher the PSNR, SSIM, and CLIP-Score, the better, and the lower the LPIPS, FID, and DISTS, the better.

Evaluation. We utilize two public benchmarks to evaluate the performance of real-world image super-resolution methods, including the real-world dataset RealSR [28] and DRealSR [31] captured by digital single-lens reflex cameras (DSLRs). To further improve the diversity and quantity of real degradation scenarios, we have collected 891 pairs of data captured by smartphones for evaluation, denoted as SmartPhone.

³<https://github.com/XPixelGroup/BasicSR>

Table 1: Quantitative comparisons of PSNR-oriented and Perceptual-oriented training SR models on three real-world image super-resolution benchmarks. The best results are highlighted in **bold**.

PSNR-oriented Training	RealSR [28]		DRealSR [31]		SmartPhone	
	PSNR \uparrow	SSIM \uparrow	PSNR \uparrow	SSIM \uparrow	PSNR \uparrow	SSIM \uparrow
SwinIR (Real-ESRGAN [33])	24.395	0.7760	26.944	0.8308	27.395	0.8338
SwinIR (BSRGAN [32])	25.852	0.7808	27.985	0.8308	28.049	0.8407
SwinIR (SynDiff [46])	25.589	0.7687	28.301	0.8309	28.566	0.8453
SwinIR (Ours)	26.094	0.7822	28.721	0.8341	28.737	0.8489
RRDB (Real-ESRGAN [33])	24.579	0.7614	27.131	0.8193	27.841	0.8378
RRDB (BSRGAN [32])	25.406	0.7685	27.523	0.8017	28.029	0.8278
RRDB (SynDiff [46])	25.488	0.7691	28.078	0.8257	28.303	0.8426
RRDB (Ours)	26.238	0.7747	28.727	0.8340	28.754	0.8507
HAT (Real-ESRGAN [33])	24.893	0.7726	27.339	0.8215	27.781	0.8336
HAT (BSRGAN [32])	25.997	0.7816	28.135	0.8273	28.137	0.8369
HAT (SynDiff [46])	25.790	0.7584	28.506	0.8286	28.508	0.8471
HAT (Ours)	26.140	0.7832	28.802	0.8345	28.767	0.8489
SwinIR-L (Real-ESRGAN [33])	24.367	0.7723	27.018	0.8244	27.581	0.8409
SwinIR-L (BSRGAN [32])	25.651	0.7800	27.813	0.8301	28.118	0.8437
SwinIR-L (SynDiff [46])	25.281	0.7516	28.170	0.8244	28.474	0.8487
SwinIR-L (Ours)	26.025	0.7810	28.869	0.8328	28.868	0.8522
Perceptual-oriented Training	RealSR[28]		DRealSR[31]		SmartPhone	
	LPIPS \downarrow	FID \downarrow	LPIPS \downarrow	FID \downarrow	LPIPS \downarrow	FID \downarrow
SwinIR (Real-ESRGAN [33])	0.3037	69.965	0.3219	39.175	0.4053	78.242
SwinIR (BSRGAN [32])	0.2945	79.833	0.3023	38.541	0.3043	76.871
SwinIR (SynDiff [46])	0.3835	103.179	0.3801	54.588	0.3129	83.485
SwinIR (Ours)	0.2536	69.736	0.2660	38.257	0.2964	74.778
RRDB (Real-ESRGAN [33])	0.3480	82.056	0.3551	39.310	0.3480	77.573
RRDB (BSRGAN [32])	0.3041	77.412	0.3127	36.528	0.3381	78.812
RRDB (SynDiff [46])	0.4004	98.798	0.4017	56.573	0.3511	88.431
RRDB (Ours)	0.2972	76.973	0.3077	36.259	0.3125	76.723
HAT (Real-ESRGAN [33])	0.3066	79.209	0.3219	41.862	0.4022	87.950
HAT (BSRGAN [32])	0.2852	80.192	0.2835	41.723	0.3049	81.247
HAT (SynDiff [46])	0.3332	93.763	0.3465	50.808	0.3171	85.587
HAT (Ours)	0.2457	67.573	0.2587	41.319	0.2816	76.873
SwinIR-L (Real-ESRGAN [33])	0.3108	79.491	0.3234	42.986	0.4021	87.531
SwinIR-L (BSRGAN [32])	0.3013	84.195	0.2978	43.246	0.3146	83.444
SwinIR-L (SynDiff)	0.3793	98.646	0.3748	52.464	0.3190	80.708
SwinIR-L (Ours)	0.2795	75.779	0.2862	42.542	0.3047	78.632

3.2 Quantitative Results

Generalization Ability of Real SR Models. We compare our method with the existing data generation methods on both PSNR-oriented and Perceptual-oriented Real SR models to validate the superiority of our method in boosting the generalization capabilities for real-world image super-resolution, and the results are shown in Tab. 1. We can observe that our method comprehensively improves the performance of PSNR-oriented and Perceptual-oriented SR models across three benchmarks. It’s worth noting that our approach achieves a significant performance improvement, including 0.75 dB in RRDB [54] on the PSNR of the RealSR benchmark; 0.296dB and 0.699 dB in SwinIR [55] and light-weight SwinIR-L on the PSNR of the RealSR benchmark. Furthermore, our methods also significantly improve LPIPS and FID in four SR models, including 0.0395 and 12.619 in HAT [56] on the LPIPS and FID of RealSR benchmark. This demonstrates that our method effectively improves the generalization capacity of popular SR models.

Accuracy of Generated Real LR. To validate our method’s superiority in generating accurately realistic and matched real LR, we conduct comparisons with existing methods in terms of the accuracy

Table 2: Quantitative comparisons of the accuracy of generating real LR images on three real-world benchmarks under six distinct similarity metrics.

Benchmark	Methods	PSNR \uparrow	SSIM \uparrow	LPIPS \downarrow	FID \downarrow	DISTS \downarrow	CLIP-Score \uparrow
RealSR [28]	Real-ESRGAN [33]	24.3974	0.6798	0.3881	157.5237	0.2618	0.7552
	BSRGAN [32]	23.2665	0.6043	0.5093	177.9996	0.3048	0.6783
	SynDiff [46]	25.2461	0.7588	0.2371	119.9950	0.1944	0.7984
	Ours	26.1615	0.7940	0.2226	107.2375	0.1865	0.8238
DRealSR [31]	RealESRGAN [33]	26.3510	0.6935	0.3842	60.2665	0.2437	0.7710
	BSRGAN [32]	26.1970	0.6869	0.4319	62.9189	0.2646	0.7137
	SynDiff [46]	28.0125	0.8136	0.1739	31.0855	0.1673	0.8462
	Ours	28.6629	0.8360	0.1497	30.0078	0.1567	0.8577
SmartPhone	RealESRGAN [33]	26.0680	0.5981	0.5202	106.3958	0.2855	0.7231
	BSRGAN [32]	27.6215	0.7179	0.4399	105.3289	0.2760	0.6771
	SynDiff [46]	28.5020	0.8075	0.2423	70.6379	0.2044	0.8213
	Ours	29.0054	0.8292	0.2121	69.1162	0.1964	0.8334

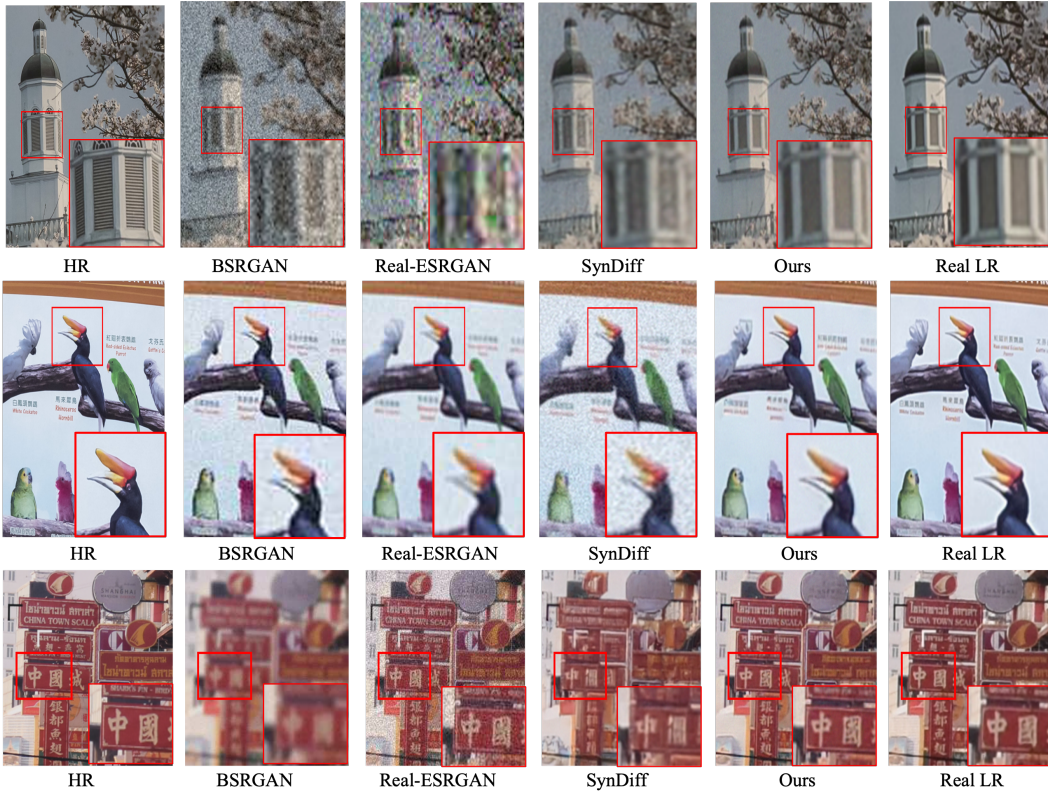


Figure 3: Visual comparison of generated LR. Our method achieves the best visual results with realistic degradation and high fidelity. Please zoom in for better visualization.

of the generated data on six metrics for evaluation. Specifically, we utilize HR images in the three real-world datasets as the content reference and employ the existing methods to synthesize generated LR images, while our method is further able to utilize the degradation reference from real LR. As shown in Tab. 2, we can observe that our method achieves the best performance on three datasets under six metrics, including distribution distance metric: FID, image structure and texture similarity metric: DISTS, and perceptual metric: LPIPS and CLIP-score, *etc.* It demonstrates the superiority of our Decoupled DDPM and verifies that our generation method is closer to target real LR images.

Generalization Ability on Out-of-distribution Data. Although we have collected about 152,000 real LR images for training, unseen scenarios often arise in real-world applications. To further explore our generalization capabilities on out-of-distribution data, we randomly extract 200 images from

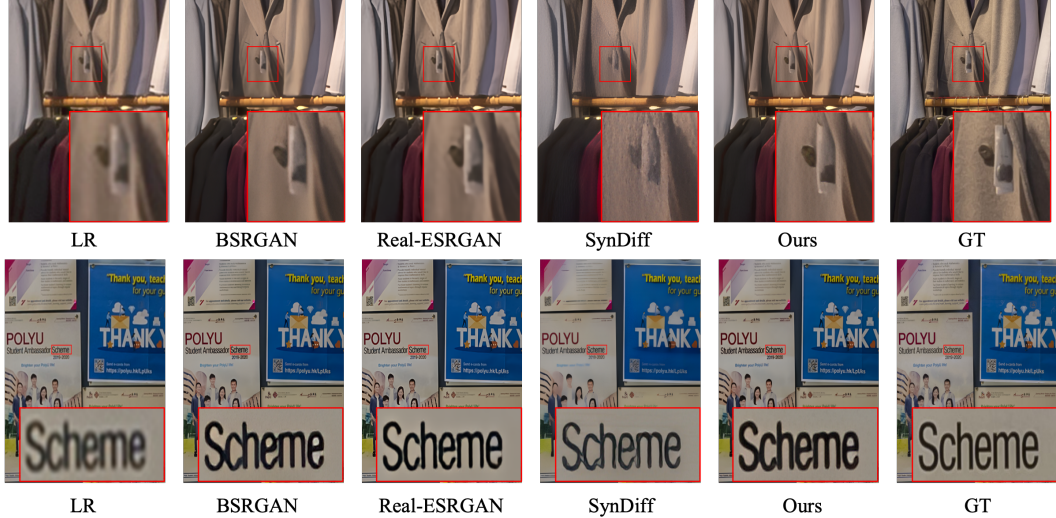


Figure 4: Visual comparison of Real SR based on different data generation methods. Real SR training using our data achieves the best visual results. Please zoom in for better visualization.

T	0-200	0-300	0-400	0-500
PSNR \uparrow	28.762	28.868	28.542	26.713
SSIM \uparrow	0.8501	0.8522	0.8435	0.7931

Table 3: Ablation study on T in our proposed Decoupled DDPM during inferencing.

Method	w/o E_{deg}	w/o E_{cont}	Ours
PSNR \uparrow	21.642	25.745	28.868
SSIM \uparrow	0.7432	0.8095	0.8522

Table 4: Ablation study on degradation extractor E_{deg} and content extractor E_{cont} .

the unseen real-world video SR data [64] for evaluation, denoted as RealVSR. Then, we capture the degradation representing those images to generate the training data and compare it with existing methods on the SwinIR-L model, and the results are shown in Tab. 5. We can observe that our method still achieves the best performance on the out-of-distribution RealVSR benchmark, surpassing the existing state-of-the-art methods by 0.2214 and 0.0055 in PSNR and SSIM, respectively. This demonstrates the ability of our method to generalize for unseen scenarios in the real world.

3.3 Qualitative Results

We visualize the results of the generated LR images, as shown in Figure 3. It is clear that the Real-ESRGAN and BSRGAN, which are unable to perceive real degradation, exhibit a significant gap compared to real LR images. The SynDiff also struggles to adaptively capture the real degradation and content representation, resulting in unreal degradation distribution and low fidelity, as shown in the third row in Figure 3. However, benefiting from our adaptive perception ability of the degradation of real LR image and content of HR image, our RealDGen achieves the best visual effect in terms of both the realism of degradation and the fidelity of content. Furthermore, to demonstrate the visual effects of Real SR model, we conduct visualizations of the SwinIR model in the RealSR and DRealSR benchmarks, as shown in Figure 4. It is clear that models based on SynDiff, BSRGAN, and Real-ESRGAN exhibit artifacts and blur. However, our method achieves the best visual quality without artifacts. The textual scene in the second row of Figure 4 also demonstrates the superiority of our method for text texture. This showcases the superior visual effects of our method in real-world scenarios. More visual comparison results are presented in Section A.7 of the appendix.

3.4 Ablation Study

Degradation and Content Extractor. Our core idea is utilizing the degradation extractor E_{deg} and content extractor E_{cont} to extract degradation and content representation to control Decoupled DDPM in generating realistic LR. To verify this, we eliminate components E_{deg} and E_{cont} , subsequently

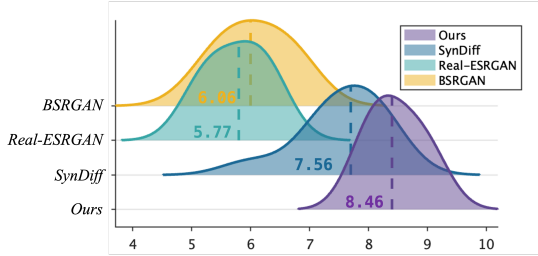


Figure 5: User study of generated real LR.

RealVSR	PSNR \uparrow	SSIM \uparrow
Real-ESRGAN [33]	22.7402	0.6939
BSRGAN [32]	22.6564	0.6779
SynDiff [46]	22.4607	0.6704
Ours	22.9616	0.6994

Table 5: The performance comparison with existing data generation method on out-of-distribution RealVSR benchmark.

training the decoupled DDPM and fine-tuning the remaining extractor. For quick evaluation, we employ SwinIR-L as the baseline and evaluate on the Smartphone benchmark. The results in Tab. 4 demonstrate that the absence of E_{deg} and E_{cont} will cause mismatch and unreal degradation and content distortion problems and result in performance degradation, thereby affirming the indispensability of E_{deg} and E_{cont} in our method.

T in Data Generation. As illustrated in Sec. 2.3, in inferencing, we denoise from an initial LR image \mathbf{x}_t with t step noise added and perform t steps of denoising to improve the fidelity of Decouple DDPM, where t is selected from the range of 0 to T . To explore it, we set T to 200, 300, 400, and 500 and conduct ablation experiments, as presented in Tab. 3. It is observed that the optimal T is 300. A lower T will result in insufficient generation of degradation, while a high T will lead to a decrease in image fidelity. Moreover, we posit that the value of T should not be a manual set but rather a variable that correlates with the degradation process. In future work, we will consider proposing the auto-selection mechanism of T that is specific to the degradation characteristics of given real LR and HR images, enhancing the controllability and fidelity of the model.

3.5 User study

To demonstrate the superiority of RealDGen in generating accurate and realistic low-resolution images, we conduct a user study involving 10 real-world LR images randomly chosen from existing benchmarks. 10 volunteers are asked to rate each scene individually (0: not similar at all; 2: not very similar; 4: slightly similar; 6: moderately similar; 8: similar; 10: extremely similar). Then, we aggregate the scores from all volunteers, and the results are shown in Figure 5. We can observe that the previous methods are unable to adaptively and accurately perceive real degradation, resulting in low fidelity in the generated real LR data, which leads to a general perception among users that there is a significant gap compared to real LR images. However, our RealDGen can adaptively capture the real degradation to accurately generate realistic LR images, resulting in an average score of 8.46 from human evaluators, surpassing previous approaches and thereby highlighting the improved visual quality that our method offers.

4 Conclusion

In this paper, we introduce a novel RealDGen to adaptively generate large-scale, high-quality paired data with arbitrary real LR as degradation reference and unpaired HR as content reference. Well-designed extractors and strategies are proposed to facilitate the extraction of robust content and degradation representations. A content-degradation decoupled diffusion model is proposed to adaptively generate realistic LR with given unpaired LR and HR conditions. Extensive experiments demonstrate that RealDGen not only achieves the best performance in generating realistic and accurate real LR images but also comprehensively improves the generalization ability of various popular SR models on real-world benchmarks. In addition, benefiting from the unsupervised learning of our method and the convenience of real LR image collection, it is easy to collect more real LR images with various real degradations to enhance generalization capability further.

Limitation: Due to the high stochasticity in the diffusion model, RealDGen sometimes finds it difficult to preserve tiny textures. In future work, we will incorporate perceptual loss for training and propose the auto-selection mechanism of the denoise step to perceive different given degradation images for further improving controllability and fidelity.

A Appendix

A.1 Training detail of Content and Degradation Extractor

we initially contemplate leveraging the auto-regressive architecture of VQGAN [65] as our Content Extractor E_{cont} to capture content representations. However, our experimental endeavors reveal that the Generative Adversarial Network (GAN) in VQGAN impedes fine-tuning and the extraction of realistic content representations. Consequently, we elect to employ the encoder component of VQVAE [66] as E_{cont} . Given that these extractors have not been trained on degradation scenarios, they are not immediately suitable for our method. To surmount this challenge, we have meticulously crafted a fine-tuning strategy predicated on reconstruction learning. Specifically, we adopt Real-ESRGAN to degrade high-resolution (HR) images to generate paired datasets for training. During training, we maintain the decoder of VQVAE in a frozen state while fine-tuning the encoder, using HR images for supervised learning, with the objective loss function being the L2 Loss. Our fine-tuning regimen is conducted with a learning rate of 1×10^{-5} , utilizing 8 NVIDIA V100 GPUs, which spent approximately one week for training. The reconstructed samples rendered by our fine-tuned Content Extractor are delineated in Fig. 6. It is evident that after fine-tuning, VQVAE adeptly captures content representations in degraded scenarios and adeptly reconstructs high-resolution images.



Figure 6: Visual comparison with Input LR image, VQVAE, our pretrained VQVAE, and GT. VQVAE, after training on our designed learning strategy, can better capture the robust content representations to reconstruct high-quality HR.

We introduce a novel Degradation Extractor denoted as E_{deg} , which is comprised of a feature extraction layer integrated with 16 residual blocks and a mapping function facilitated by adaptive pooling and a 4-layer convolutional structure, as shown in Fig. 7. Specifically, given the input of a low-resolution image into the Degradation Extractor, it engenders the output degradation representation $F_{deg} \in \mathbb{R}^{1 \times 1 \times 2048}$. To ensure the extraction of comprehensive and unique degradation representations in the LR image, we employ both reconstruction learning and contrastive learning methodologies in training our network. The training is executed on 8 NVIDIA V100 GPUs over the course of approximately seven days, with the learning rate configured at $1e - 4$.

A.2 Detail of HR and LR Reconstruction Network

To better adapt to the content extractor, that is, the encoder of the VQVAE, the decoder of VQVAE is adopted as HR reconstruction network Rec_{hr} tasked with the reconstruction of high-resolution images. Given that the LR reconstruction network is tasked with reconstructing the LR image from

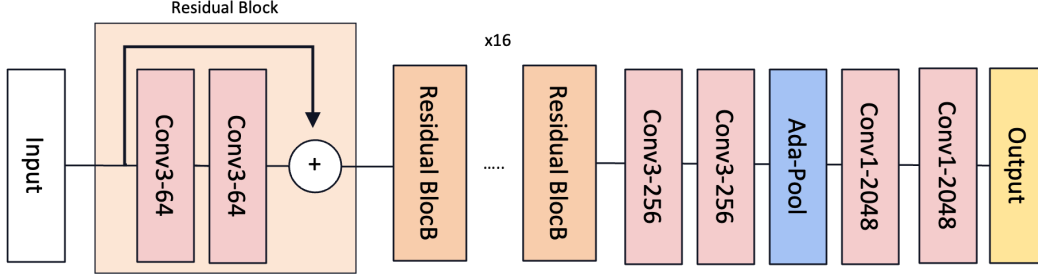


Figure 7: Illustration of our proposed degradation extractor.

content and degradation representations, we have adopted the aforementioned modulation network as our LR reconstruction network Rec_{lr} .

A.3 Training Details of Decouple DDPM

During the training of the Decoupled DDPM, we configure the maximum diffusion step to be 500, span the training over 100 epochs, and utilize a learning rate of $1e - 4$ for the decoupled diffusion model. For the fine-tuning of the extractors, we apply a more refined learning rate of $1e - 6$. The batch size is defined as 8, and the entire training regimen is on 8 NVIDIA V100 GPUs, which typically consume around 14 days to complete.

We have amassed a collection of approximately 152,000 real low-resolution images sourced from publicly available datasets such as [31, 28, 49] and those captured using smartphones. To elaborate, we have extracted all low-resolution images from these datasets and have cropped each to a uniform size of 256×256 , resulting in a total of 110,000 images. Subsequently, to enhance the diversity of real-world degradation distribution, we have additionally procured 42,000 low-resolution images, each of the same 256×256 size. Collectively, this corpus of 152,000 low-resolution images serves as the training data for our Decoupled DDPM.

A.4 Detail of Modulation Block

As detailed in Section 2, we commence with real low-resolution images, denoted as \mathcal{X}_r , which are derived from the real-world degradation distribution q . Utilizing our pre-trained extractors E_{cont} and E_{deg} , we meticulously extract the respective content and degradation representations, F_{cont} and F_{deg} . To authentically emulate the intricacies of the real imaging process, we introduce a modulation block, denoted as \mathcal{M} , which seamlessly integrates the degradation representation into the content representation. The integration is mathematically articulated as follows:

$$\mathbf{c} = \mathcal{M}(E_{deg}(\mathbf{x}_{lr}), E_{cont}(\mathbf{x}_{hr})) \quad (8)$$

In this section, we proceed to elucidate the intricate mechanisms underpinning the modulation block \mathcal{M} . \mathcal{M} is meticulously constructed from a series of four modulation layers, each comprising a convolutional layer, an activation function, and a modulation unit, as shown in Fig. 8. The inputs to \mathcal{M} encompass both the degradation and content representations. Within each modulation unit, the degradation representation is subjected to a sophisticated fusion process. Ultimately, the block culminates in its output through a final convolutional operation, synthesizing the enhanced representation.

A.5 Analysis and Details of Fine-Tuning Extractor

During the second phase of training, we froze the majority of parameters in the content extractor, allowing only the first block within the VQVAE to undergo fine-tuning. Simultaneously, we applied a similar approach to the degradation extractor, restricting fine-tuning to the final convolutional layer. To validate the effectiveness of fine-tuning, we conduct an ablation experiment. In the second phase, we completely freeze the extractor and train only the Decoupled DDPM. We find that the realism of the generated degradation decreases because the extractor is trained exclusively on synthetic datasets, which results in its inability to extract real degradation representations and content. Consequently,

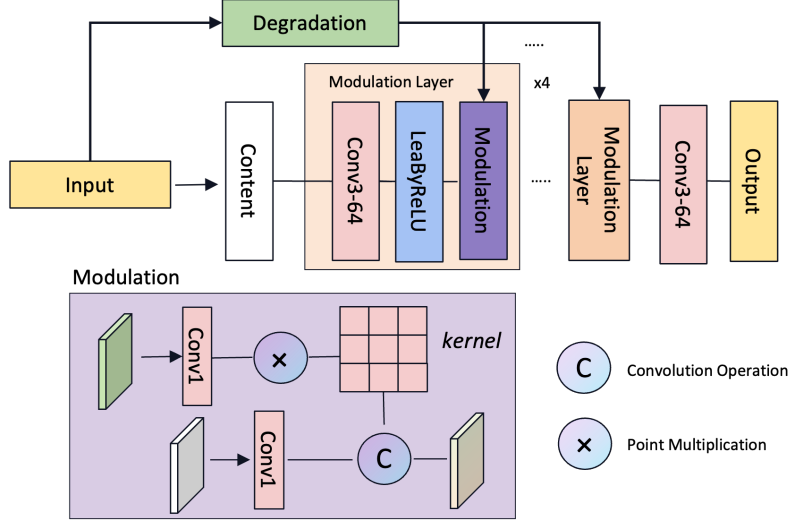


Figure 8: Illustration of our modulation block.

the subsequent DDPM also has difficulty fitting the real LR accurately. Specifically, we test on the RealSR dataset using SwinIR-L, resulting in a 0.25dB performance degradation in PSNR with fine-tuning.

A.6 Stochasticity of Diffusion

As discussed in Sec. 4, to mitigate the stochasticity of diffusion, we propose a filtering mechanism to eliminate outlier data. To validate this, we conduct experiments on the RealSR dataset, calculating the similarity and data distribution compared to the real LR images in RealSR. Additionally, we verify the effectiveness using the downstream SR network SwinIR-L, with results presented in Tables 6 and 7. It can be observed that the data generated without the filtering mechanism exhibits lower similarity and further divergence from the real LR images, as well as reduced performance in the downstream SR network. This confirms the effectiveness and practicality of our proposed filtering mechanism in real-world scenarios.

RealSR	PSNR \uparrow	SSIM \uparrow	LPIPS \downarrow	FID \downarrow
w/o Filtering	25.8965	0.7886	0.2316	116.8970
Ours	26.1615	0.7940	0.2226	107.2375

Table 6: The similarity results of ablation study on proposed filtering mechanic.

SwinIR-L	PSNR \uparrow	SSIM \uparrow
w/o Filtering	25.8747	0.7783
Ours	26.0250	0.7810

Table 7: The performance of SwinIR-L on RealSR benchmark.

A.7 More Visual Comparison

Here, we present more visual results on the DRealSR benchmark to demonstrate the superiority of our method in adaptively generating accurate and realistic LR images, as shown in Fig. 9 and 10.

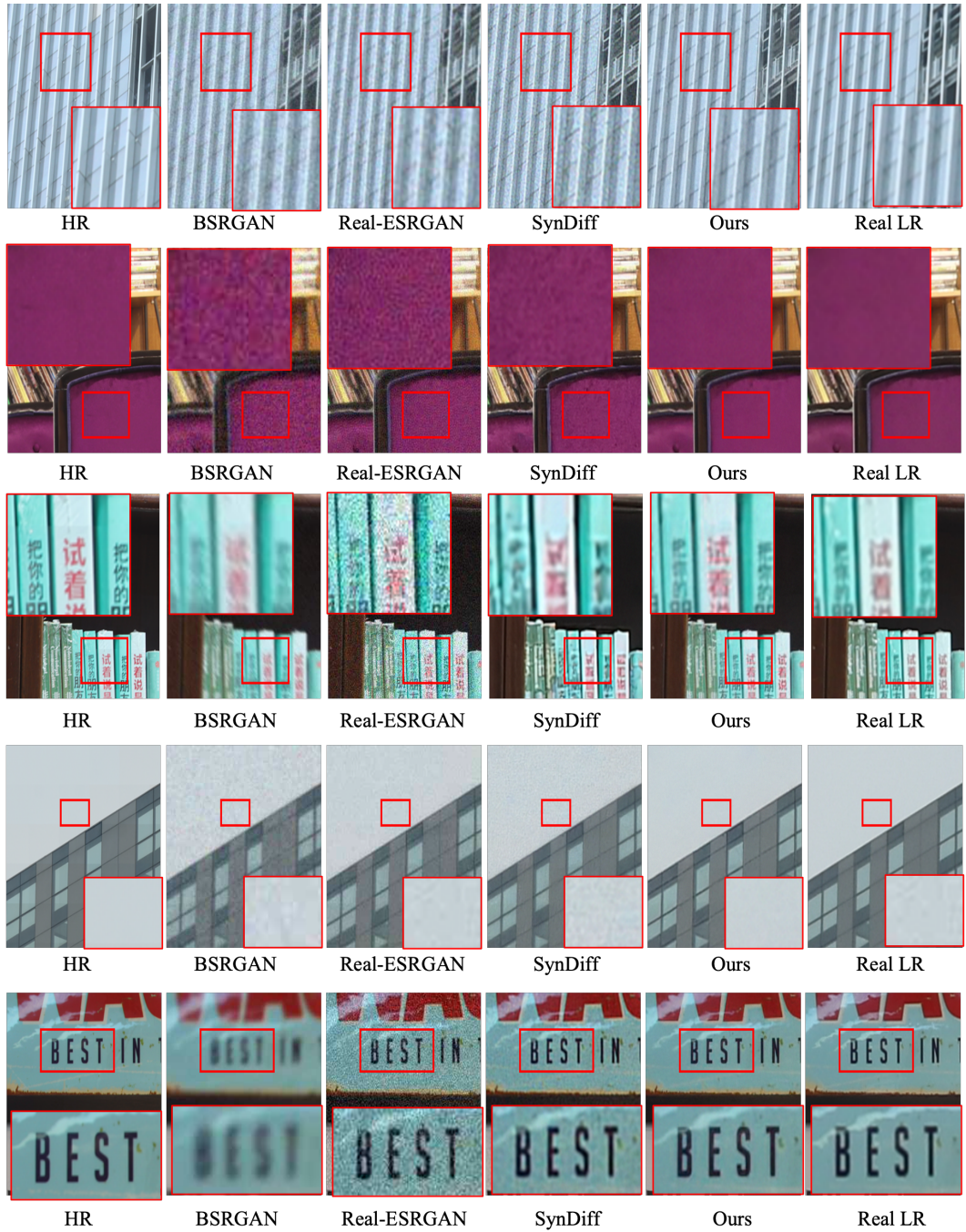


Figure 9: Visual comparison of generated LR on DRealSR.

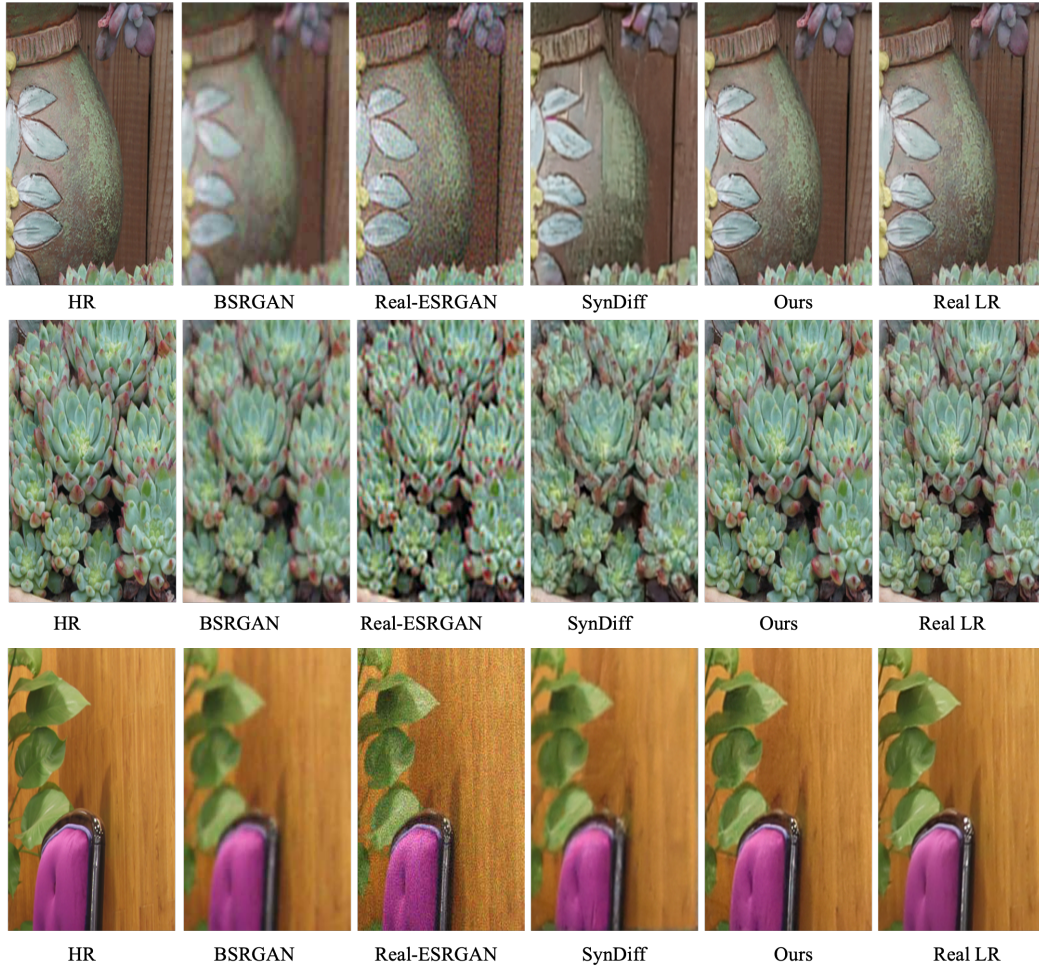


Figure 10: Visual comparison of generated LR on DRealSR.

References

- [1] Honggang Chen, Xiaohai He, Linbo Qing, Yuanyuan Wu, Chao Ren, Ray E Sheriff, and Ce Zhu. Real-world single image super-resolution: A brief review. *Information Fusion*, 79:124–145, 2022.
- [2] Fanghua Yu, Jinjin Gu, Zheyuan Li, Jinfan Hu, Xiangtao Kong, Xintao Wang, Jingwen He, Yu Qiao, and Chao Dong. Scaling up to excellence: Practicing model scaling for photo-realistic image restoration in the wild. *arXiv preprint arXiv:2401.13627*, 2024.
- [3] Yihao Liu, Hengyuan Zhao, Jinjin Gu, Yu Qiao, and Chao Dong. Evaluating the generalization ability of super-resolution networks. *IEEE Transactions on pattern analysis and machine intelligence*, 2023.
- [4] Wenlong Zhang, Xiaohui Li, Xiangyu Chen, Xiaoyun Zhang, Yu Qiao, Xiao-Ming Wu, and Chao Dong. Seal: A framework for systematic evaluation of real-world super-resolution. In *The Twelfth International Conference on Learning Representations*, 2023.
- [5] Haoze Sun, Wenbo Li, Jianzhuang Liu, Haoyu Chen, Renjing Pei, Xueyi Zou, Youliang Yan, and Yujiu Yang. Coser: Bridging image and language for cognitive super-resolution. *arXiv preprint arXiv:2311.16512*, 2023.
- [6] Wenlong Zhang, Xiaohui Li, Guangyuan Shi, Xiangyu Chen, Yu Qiao, Xiaoyun Zhang, Xiao-Ming Wu, and Chao Dong. Real-world image super-resolution as multi-task learning. *Advances in Neural Information Processing Systems*, 36, 2024.
- [7] Du Chen, Jie Liang, Xindong Zhang, Ming Liu, Hui Zeng, and Lei Zhang. Human guided ground-truth generation for realistic image super-resolution. In *Proceedings of the IEEE/CVF Conference on Computer Vision and Pattern Recognition*, pages 14082–14091, 2023.
- [8] Yan Huang, Shang Li, Liang Wang, Tieniu Tan, et al. Unfolding the alternating optimization for blind super resolution. *Advances in Neural Information Processing Systems*, 33:5632–5643, 2020.
- [9] Andreas Lugmayr, Martin Danelljan, and Radu Timofte. Ntire 2020 challenge on real-world image super-resolution: Methods and results. In *Proceedings of the IEEE/CVF Conference on Computer Vision and Pattern Recognition Workshops*, pages 494–495, 2020.
- [10] Wenbo Li, Kun Zhou, Lu Qi, Liying Lu, and Jiangbo Lu. Best-buddy gans for highly detailed image super-resolution. In *Proceedings of the AAAI Conference on Artificial Intelligence*, volume 36, pages 1412–1420, 2022.
- [11] Andreas Lugmayr, Martin Danelljan, and Radu Timofte. Unsupervised learning for real-world super-resolution. In *2019 IEEE/CVF International Conference on Computer Vision Workshop (ICCVW)*, pages 3408–3416. IEEE, 2019.
- [12] Xiaozhong Ji, Yun Cao, Ying Tai, Chengjie Wang, Jilin Li, and Feiyue Huang. Real-world super-resolution via kernel estimation and noise injection. In *proceedings of the IEEE/CVF conference on computer vision and pattern recognition workshops*, pages 466–467, 2020.
- [13] Chong Mou, Yanze Wu, Xintao Wang, Chao Dong, Jian Zhang, and Ying Shan. Metric learning based interactive modulation for real-world super-resolution. In *European Conference on Computer Vision*, pages 723–740. Springer, 2022.
- [14] Anran Liu, Yihao Liu, Jinjin Gu, Yu Qiao, and Chao Dong. Blind image super-resolution: A survey and beyond. *IEEE Transactions on Pattern Analysis and Machine Intelligence*, 2022.
- [15] Manuel Fritsche, Shuhang Gu, and Radu Timofte. Frequency separation for real-world super-resolution. In *2019 IEEE/CVF International Conference on Computer Vision Workshop (ICCVW)*, pages 3599–3608. IEEE, 2019.
- [16] Yuanbo Zhou, Wei Deng, Tong Tong, and Qinquan Gao. Guided frequency separation network for real-world super-resolution. In *Proceedings of the IEEE/CVF Conference on Computer Vision and Pattern Recognition Workshops*, pages 428–429, 2020.
- [17] Longguang Wang, Yingqian Wang, Xiaoyu Dong, Qingyu Xu, Jungang Yang, Wei An, and Yulan Guo. Unsupervised degradation representation learning for blind super-resolution. In *Proceedings of the IEEE/CVF Conference on Computer Vision and Pattern Recognition*, pages 10581–10590, 2021.

- [18] Chang Chen, Zhiwei Xiong, Xinmei Tian, Zheng-Jun Zha, and Feng Wu. Camera lens super-resolution. In *Proceedings of the IEEE/CVF Conference on Computer Vision and Pattern Recognition*, pages 1652–1660, 2019.
- [19] Andreas Lugmayr, Martin Danelljan, Radu Timofte, Manuel Fritsche, Shuhang Gu, Kuldeep Purohit, Praveen Kandula, Maitreya Suin, AN Rajagoapalan, Nam Hyung Joon, et al. Aim 2019 challenge on real-world image super-resolution: Methods and results. In *2019 IEEE/CVF International Conference on Computer Vision Workshop (ICCVW)*, pages 3575–3583. IEEE, 2019.
- [20] Jianrui Cai, Shuhang Gu, Radu Timofte, and Lei Zhang. Ntire 2019 challenge on real image super-resolution: Methods and results. In *Proceedings of the IEEE/CVF Conference on Computer Vision and Pattern Recognition Workshops*, pages 0–0, 2019.
- [21] Long Peng, Yang Cao, Renjing Pei, Wenbo Li, Jiaming Guo, Xueyang Fu, Yang Wang, and Zheng-Jun Zha. Efficient real-world image super-resolution via adaptive directional gradient convolution. *arXiv preprint arXiv:2405.07023*, 2024.
- [22] Marcos V Conde, Zhijun Lei, Wen Li, Cosmin Stejerean, Ioannis Katsavounidis, Radu Timofte, Kihwan Yoon, Ganzorig Gankhuyag, Jiangtao Lv, Long Sun, et al. Real-time 4k super-resolution of compressed avif images. ais 2024 challenge survey. *arXiv preprint arXiv:2404.16484*, 2024.
- [23] Y Li, Bruno Sixou, and F Peyrin. A review of the deep learning methods for medical images super resolution problems. *Irbm*, 42(2):120–133, 2021.
- [24] Muhammad Haris, Greg Shakhnarovich, and Norimichi Ukita. Task-driven super resolution: Object detection in low-resolution images. In *Neural Information Processing: 28th International Conference, ICONIP 2021, Sanur, Bali, Indonesia, December 8–12, 2021, Proceedings, Part V* 28, pages 387–395. Springer, 2021.
- [25] Dewan Fahim Noor, Yue Li, Zhu Li, Shuvra Bhattacharyya, and George York. Gradient image super-resolution for low-resolution image recognition. In *ICASSP 2019-2019 IEEE International Conference on Acoustics, Speech and Signal Processing (ICASSP)*, pages 2332–2336. IEEE, 2019.
- [26] Bahadır K Gunturk, Aziz Umit Batur, Yucel Altunbasak, Monson H Hayes, and Russell M Mersereau. Eigenface-domain super-resolution for face recognition. *IEEE transactions on image processing*, 12(5):597–606, 2003.
- [27] Jin Chen, Jun Chen, Zheng Wang, Chao Liang, and Chia-Wen Lin. Identity-aware face super-resolution for low-resolution face recognition. *IEEE Signal Processing Letters*, 27:645–649, 2020.
- [28] Jianrui Cai, Hui Zeng, Hongwei Yong, Zisheng Cao, and Lei Zhang. Toward real-world single image super-resolution: A new benchmark and a new model. In *Proceedings of the IEEE/CVF International Conference on Computer Vision*, pages 3086–3095, 2019.
- [29] Zhihao Wang, Jian Chen, and Steven CH Hoi. Deep learning for image super-resolution: A survey. *IEEE transactions on pattern analysis and machine intelligence*, 43(10):3365–3387, 2020.
- [30] Haoyu Chen, Wenbo Li, Jinjin Gu, Jingjing Ren, Haoze Sun, Xueyi Zou, Zhensong Zhang, Youliang Yan, and Lei Zhu. Low-res leads the way: Improving generalization for super-resolution by self-supervised learning. *arXiv preprint arXiv:2403.02601*, 2024.
- [31] Pengxu Wei, Ziwei Xie, ZongYuan Zhan Hannan Lu, Qixiang Ye, Wangmeng Zuo, and Liang Lin. Component divide-and-conquer for real-world image super-resolution. In *Proceedings of the European Conference on Computer Vision*, 2020.
- [32] Kai Zhang, Jingyun Liang, Luc Van Gool, and Radu Timofte. Designing a practical degradation model for deep blind image super-resolution. In *Proceedings of the IEEE/CVF International Conference on Computer Vision*, pages 4791–4800, 2021.
- [33] Xintao Wang, Liangbin Xie, Chao Dong, and Ying Shan. Real-esrgan: Training real-world blind super-resolution with pure synthetic data. In *Proceedings of the IEEE/CVF international conference on computer vision*, pages 1905–1914, 2021.
- [34] Ruofan Zhang, Jinjin Gu, Haoyu Chen, Chao Dong, Yulun Zhang, and Wenming Yang. Crafting training degradation distribution for the accuracy-generalization trade-off in real-world super-resolution. In *International Conference on Machine Learning*, pages 41078–41091. PMLR, 2023.

- [35] Seobin Park, Dongjin Kim, Sungyong Baik, and Tae Hyun Kim. Learning controllable degradation for real-world super-resolution via constrained flows. In *International Conference on Machine Learning*, pages 27188–27203. PMLR, 2023.
- [36] Xiaoming Li, Chaofeng Chen, Xianhui Lin, Wangmeng Zuo, and Lei Zhang. From face to natural image: Learning real degradation for blind image super-resolution. In *European Conference on Computer Vision*, pages 376–392. Springer, 2022.
- [37] Jin Xiao, Hongwei Yong, and Lei Zhang. Degradation model learning for real-world single image super-resolution. In *Proceedings of the Asian Conference on Computer Vision*, 2020.
- [38] Valentin Wolf, Andreas Lugmayr, Martin Danelljan, Luc Van Gool, and Radu Timofte. Deflow: Learning complex image degradations from unpaired data with conditional flows. In *Proceedings of the IEEE/CVF Conference on Computer Vision and Pattern Recognition*, pages 94–103, 2021.
- [39] Michael Elad and Arie Feuer. Restoration of a single superresolution image from several blurred, noisy, and undersampled measured images. *IEEE transactions on image processing*, 6(12):1646–1658, 1997.
- [40] Chao Dong, Chen Change Loy, and Xiaoou Tang. Accelerating the super-resolution convolutional neural network. In *Computer Vision—ECCV 2016: 14th European Conference, Amsterdam, The Netherlands, October 11–14, 2016, Proceedings, Part II 14*, pages 391–407. Springer, 2016.
- [41] Ioan Raicu, Yong Zhao, Ian T Foster, and Alex Szalay. Accelerating large-scale data exploration through data diffusion. In *Proceedings of the 2008 international workshop on Data-aware distributed computing*, pages 9–18, 2008.
- [42] Shunta Maeda. Unpaired image super-resolution using pseudo-supervision. In *Proceedings of the IEEE/CVF Conference on Computer Vision and Pattern Recognition*, pages 291–300, 2020.
- [43] Vikash Sehwal, Caner Hazirbas, Albert Gordo, Firat Ozgenel, and Cristian Canton. Generating high fidelity data from low-density regions using diffusion models. In *Proceedings of the IEEE/CVF Conference on Computer Vision and Pattern Recognition*, pages 11492–11501, 2022.
- [44] Weijia Wu, Yuzhong Zhao, Hao Chen, Yuchao Gu, Rui Zhao, Yefei He, Hong Zhou, Mike Zheng Shou, and Chunhua Shen. Datasetdm: Synthesizing data with perception annotations using diffusion models. *Advances in Neural Information Processing Systems*, 36:54683–54695, 2023.
- [45] Adrian Bulat, Jing Yang, and Georgios Tzimiropoulos. To learn image super-resolution, use a gan to learn how to do image degradation first. In *Proceedings of the European conference on computer vision (ECCV)*, pages 185–200, 2018.
- [46] Tao Yang, Peiran Ren, Lei Zhang, et al. Synthesizing realistic image restoration training pairs: A diffusion approach. *arXiv preprint arXiv:2303.06994*, 2023.
- [47] A Lugmayr, M Danelljan, L Van Gool, and R Timofte. Learning the super-resolution space with normalizing flow. *ECCV, Srfow*, 2020.
- [48] Yuan Yuan, Siyuan Liu, Jiawei Zhang, Yongbing Zhang, Chao Dong, and Liang Lin. Un-supervised image super-resolution using cycle-in-cycle generative adversarial networks. In *Proceedings of the IEEE conference on computer vision and pattern recognition workshops*, pages 701–710, 2018.
- [49] Andrey Ignatov, Nikolay Kobyshev, Radu Timofte, Kenneth Vanhoey, and Luc Van Gool. Dslr-quality photos on mobile devices with deep convolutional networks. In *Proceedings of the IEEE international conference on computer vision*, pages 3277–3285, 2017.
- [50] Chenlin Meng, Yutong He, Yang Song, Jiaming Song, Jiajun Wu, Jun-Yan Zhu, and Stefano Ermon. Sedit: Guided image synthesis and editing with stochastic differential equations. *arXiv preprint arXiv:2108.01073*, 2021.
- [51] Jonathan Ho, Ajay Jain, and Pieter Abbeel. Denoising diffusion probabilistic models. *Advances in neural information processing systems*, 33:6840–6851, 2020.
- [52] Robin Rombach, Andreas Blattmann, Dominik Lorenz, Patrick Esser, and Björn Ommer. High-resolution image synthesis with latent diffusion models. In *Proceedings of the IEEE/CVF conference on computer vision and pattern recognition*, pages 10684–10695, 2022.
- [53] Eirikur Agustsson and Radu Timofte. Ntire 2017 challenge on single image super-resolution: Dataset and study. In *Proceedings of the IEEE conference on computer vision and pattern recognition workshops*, pages 126–135, 2017.

- [54] Xintao Wang, Ke Yu, Shixiang Wu, Jinjin Gu, Yihao Liu, Chao Dong, Yu Qiao, and Chen Change Loy. Esrgan: Enhanced super-resolution generative adversarial networks. In *Proceedings of the European conference on computer vision (ECCV) workshops*, pages 0–0, 2018.
- [55] Jingyun Liang, Jiezhong Cao, Guolei Sun, Kai Zhang, Luc Van Gool, and Radu Timofte. Swinir: Image restoration using swin transformer. In *Proceedings of the IEEE/CVF international conference on computer vision*, pages 1833–1844, 2021.
- [56] Xiangyu Chen, Xintao Wang, Jiantao Zhou, Yu Qiao, and Chao Dong. Activating more pixels in image super-resolution transformer. In *Proceedings of the IEEE/CVF Conference on Computer Vision and Pattern Recognition*, pages 22367–22377, 2023.
- [57] Justin Johnson, Alexandre Alahi, and Li Fei-Fei. Perceptual losses for real-time style transfer and super-resolution. In *Computer Vision—ECCV 2016: 14th European Conference, Amsterdam, The Netherlands, October 11–14, 2016, Proceedings, Part II 14*, pages 694–711. Springer, 2016.
- [58] Quan Huynh-Thu and Mohammed Ghanbari. Scope of validity of psnr in image/video quality assessment. *Electronics letters*, 44(13):800–801, 2008.
- [59] Zhou Wang, Alan C Bovik, Hamid R Sheikh, and Eero P Simoncelli. Image quality assessment: from error visibility to structural similarity. *IEEE transactions on image processing*, 13(4):600–612, 2004.
- [60] Richard Zhang, Phillip Isola, Alexei A Efros, Eli Shechtman, and Oliver Wang. The unreasonable effectiveness of deep features as a perceptual metric. In *Proceedings of the IEEE conference on computer vision and pattern recognition*, pages 586–595, 2018.
- [61] Martin Heusel, Hubert Ramsauer, Thomas Unterthiner, Bernhard Nessler, and Sepp Hochreiter. Gans trained by a two time-scale update rule converge to a local nash equilibrium. *Advances in neural information processing systems*, 30, 2017.
- [62] Keyan Ding, Kede Ma, Shiqi Wang, and Eero P Simoncelli. Image quality assessment: Unifying structure and texture similarity. *IEEE transactions on pattern analysis and machine intelligence*, 44(5):2567–2581, 2020.
- [63] Alec Radford, Jong Wook Kim, Chris Hallacy, Aditya Ramesh, Gabriel Goh, Sandhini Agarwal, Girish Sastry, Amanda Askell, Pamela Mishkin, Jack Clark, et al. Learning transferable visual models from natural language supervision. In *International conference on machine learning*, pages 8748–8763. PMLR, 2021.
- [64] Xi Yang, Wangmeng Xiang, Hui Zeng, and Lei Zhang. Real-world video super-resolution: A benchmark dataset and a decomposition based learning scheme. In *Proceedings of the IEEE/CVF International Conference on Computer Vision*, pages 4781–4790, 2021.
- [65] Patrick Esser, Robin Rombach, and Bjorn Ommer. Taming transformers for high-resolution image synthesis. In *Proceedings of the IEEE/CVF conference on computer vision and pattern recognition*, pages 12873–12883, 2021.
- [66] Ali Razavi, Aaron van den Oord, and Oriol Vinyals. Generating diverse high-fidelity images with vq-vae-2, 2019.